Published in final edited form as:

Neuron. 2016 April 6; 90(1): 101–112. doi:10.1016/j.neuron.2016.02.019.

Distinct Contribution of Adult-Born Hippocampal Granule Cells to Context Encoding

Nathan B. Danielson[3,4], **Patrick Kaifosh**[3,4], **Jeffrey D. Zaremba**[3,4], **Matthew Lovett-Barron**[3,6], **Joseph Tsai**[3,4], **Christine A. Denny**[1,2], **Elizabeth M. Balough**[3,4], **Alexander R. Goldberg**[2], **Liam J. Drew**[1,2,7], **René Hen**[1,2,3,5], **Attila Losonczy**[3,5,*], and **Mazen A. Kheirbek**[1,2,8,9]

[1]Department of Psychiatry, Columbia University, New York, NY 10032, USA

[2]Division of Integrative Neuroscience, New York State Psychiatric Institute, New York, NY 10032, USA

[3]Department of Neuroscience, Columbia University, New York, NY 10032, USA

[4]Doctoral Program in Neurobiology and Behavior, Columbia University, New York, NY 10032, USA

[5]Kavli Institute for Brain Science, Columbia University, New York, NY 10032, USA

[6]Department of Bioengineering, Stanford University, Stanford, CA 94305, USA

[7]Wolfson Institute for Biomedical Research, UCL, London WC1E 0BT, UK

[8]Department of Psychiatry, University of California, San Francisco, San Francisco, CA 94158, USA

[9]Center for Integrative Neuroscience, University of California, San Francisco, San Francisco, CA 94158, USA

SUMMARY

Adult-born granule cells (abGCs) have been implicated in cognition and mood; however, it remains unknown how these cells behave in vivo. Here, we have used two-photon calcium imaging to monitor the activity of young abGCs in awake behaving mice. We find that young adult-born neurons fire at a higher rate in vivo but paradoxically exhibit less spatial tuning than their mature counterparts. When presented with different contexts, mature granule cells underwent robust remapping of their spatial representations, and the few spatially tuned adult-born cells remapped to a similar degree. We next used optogenetic silencing to confirm the direct involvement of abGCs

*Correspondence: al2856@cumc.columbia.edu.

In Brief

Danielson et al. monitored and controlled the activity of adult-born and mature dentate gyrus neurons in vivo. They show that as a population, young adult-born neurons are more active and less sharply spatially tuned than their mature counterparts and that these cells contribute to context encoding.

SUPPLEMENTAL INFORMATION

Supplemental Information includes Supplemental Experimental Procedures, six figures, one table, and one movie and can be found with this article online at http://dx.doi.org/10.1016/j.neuron.2016.02.019.

AUTHOR CONTRIBUTIONS

N.B.D., R.H., A.L., and M.A.K. conceived the project, designed the experiments, and wrote the manuscript. N.B.D., P.K., J.D.Z., A.L., and M.A.K. performed experiments and analyzed data. M.L.-B., J.T., C.A.D., E.M.B., A.R.G., and L.J.D. assisted with experiments and provided essential reagents, expertise, and input to the manuscript.

in context encoding and discrimination, consistent with their proposed role in pattern separation. These results provide the first in vivo characterization of abGCs and reveal their participation in the encoding of novel information.

INTRODUCTION

Hippocampal neurogenesis in the adult mammalian brain is a process by which new dentate gyrus (DG) granule cells (GCs) are generated and functionally integrated into hippocampal circuitry (Drew et al., 2013; Toni et al., 2007, 2008; van Praag et al., 2002). In both rodents and humans, a significant fraction of DG neurons are replaced by neurons generated in adulthood (Imayoshi et al., 2008; Spalding et al., 2013). Why this is the case and precisely how young adult-born GCs (abGCs) alter hippocampal circuit function remain open questions.

Behavioral studies have implicated abGCs in memory formation (Zhao et al., 2008); stress and anxiety (Snyder et al., 2011); responses to antidepressant treatments (David et al., 2009; Santarelli et al., 2003); and, most recently, in behaviors requiring contextual discrimination, consistent with a role in pattern separation (Clelland et al., 2009; Kheirbek et al., 2012a; Nakashiba et al., 2012; Sahay et al., 2011a). However, such studies have primarily inferred functions of abGCs from experiments in which adult neurogenesis was chronically ablated or enhanced, i.e., long-term manipulations that may induce compensatory changes (Singer et al., 2011) and/or result in the recruitment of alternative behavioral or cognitive strategies. Furthermore, in these designs abGCs are either absent or more abundant during all phases of testing.

Hypotheses attempting to explain the role of abGCs range from modulating the activity of mature GCs (mGCs) through interactions with local interneurons, to themselves providing the DG's principal output signals (Piatti et al., 2013; Sahay et al., 2011b). Brain slice preparations have provided additional insight into the possible mechanisms by which they may uniquely influence circuit function (Dieni et al., 2013; Marín-Burgin et al., 2012; Temprana et al., 2015; van Praag et al., 2002). For example, adult-born neurons undergo a period of heightened synaptic plasticity 4–6 weeks postmitosis, a critical period during which they have been proposed to have a distinct contribution to behavior (Denny et al., 2012; Ge et al., 2007; Kheirbek et al., 2012b; Schmidt-Hieber et al., 2004). Further observed differences in excitability and plasticity could allow abGCs to encode and transfer information differently than mGCs (Ge et al., 2007; Gu et al., 2012; Schmidt-Hieber et al., 2004; van Praag et al., 2002). However, at present there are no data from the intact brain directly comparing the firing patterns of these subpopulations during behavior. This is because in vivo identification of mGCs and abGCs with electrophysiological approaches remains technically challenging (Jung and McNaughton, 1993; Leutgeb et al., 2007; Neunuebel and Knierim, 2012; Pernía-Andrade and Jonas, 2014). Studies using immediate early gene expression as a proxy for neuronal activation have not identified significant differences in the recruitment of mGCs and abGCs (Stone et al., 2011) during contextual encoding, but this methodology fails to capture the dynamic nature of neuronal encoding.

Here, we have recorded the activity of abGCs in vivo, providing the first functional characterization of identified abGCs. Although these cells are more active than mGCs in vivo, they are less spatially tuned. Furthermore, we found that mGCs robustly discriminated contexts on the basis of their spatial tuning, while the small population of spatially tuned abGCs seemed to discriminate contexts to a similar or lesser degree, depending on the inclusion criteria and remapping metric applied. We confirmed this online participation of abGCs to the encoding of novel information by transiently suppressing abGCs's activity in distinct epochs of conditioning paradigms, where we showed their essential role in behavioral pattern separation. These experiments extend our understanding of the unique contribution of abGCs to behavior and provide the first characterization of their activity in vivo.

RESULTS

Two-Photon Calcium Imaging of DG GCs In Vivo

To gain insight into how abGCs behave in vivo, we sought to directly observe their activity in the intact brain in response to the manipulation of spatial and contextual cues. This was achieved by performing calcium imaging of the DG in head-restrained mice as they explored a linear virtual environment (Kaifosh et al., 2013; Lovett-Barron et al., 2014) (Figure 1A). Use of this method allowed us to image the activity of abGCs and mGCs simultaneously, which is not yet technically feasible in freely moving mice. To label abGCs, NestinCreER^{T2} mice (Dranovsky et al., 2011) were crossed with a conditional tdTomato reporter line (*Nestin*^{tdTomato}) and pulsed with tamoxifen (TMX) 6 weeks prior to imaging. This led to labeling of 89.5% ± 3.8% of the DCX population of immature cells 6 weeks after induction, indicating ~10% of abGCs were not labeled and thus were not characterized as abGCs. Mice were stereotactically injected in the dorsal DG with a virus expressing GCaMP6f in all GCs. Implantation of a chronic imaging window over the dorsal DG provided the optical access necessary for cell-type-specific imaging of the DG GC layer (Figures 1A and S1, available online). This preparation did not impair hippocampal-dependent contextual conditioning, nor did it impact the overall level of activity in the DG. In addition, window implantation did not impact total number of tdTomato+ abGCs, their dendritic morphology, or the number of proliferating cells in the implanted hemisphere.

In total, we imaged 7,950 mGCs (tdTomato negative) and 446 abGCs (tdTomato positive) from 11 fields of view (FOVs) across 6 mice (Figure S1). The same FOV (Figure S2) was imaged over three trials in which the mouse explored two linear virtual contexts. On the first trial, the mouse explored one of the two contexts (A; chosen at random), then for both the second and third trials it explored the second context (B). This paradigm allowed us to compare activity levels, spatial firing patterns, and remapping dynamics in abGCs and mGCs simultaneously.

abGCs Are More Active Than mGCs In Vivo

Consistent with electrophysiological studies reporting sparse GC activity (Alme et al., 2010; Leutgeb et al., 2007; Pernía-Andrade and Jonas, 2014; Schmidt-Hieber et al., 2014), detected calcium transients (Figure S2A) were observed at very low rates in both abGCs and

mGCs (Figures 1B–1D; Movie S1). The level of activity was dependent on the animal's behavioral state (Leutgeb et al., 2007; Neunuebel and Knierim, 2012), as calcium transients during running were observed at nearly 2-fold higher rate than during nonrunning epochs (Figure S2C). Running-related calcium transients occurred at significantly greater rates in abGCs than in mGCs across all transients (Figures 1B and 1C) as well as across FOVs (Figure 1D). This difference was most pronounced in the FOVs that displayed the highest levels of activity. The increased activity observed in vivo is consistent with reports of greater responsiveness to perforant path activation of abGCs in vitro (Marín-Burgin et al., 2012). In addition to having a lower overall fraction of silent cells, the abGC population also contained a higher fraction of highly active cells (Figure 1C, inset). Additionally, across FOVs, we did not detect differences between mGCs and abGCs in the amplitude or duration of detected transients suggesting similar activity-induced calcium dynamics in the two populations (Figure S2B).

abGCs Are Less Spatially Tuned Than mGCs

We next assessed the degree to which abGCs and mGCs were spatially tuned (Figure 2). To limit noise in estimates of the spatial tuning metrics, we included only GC recordings with four or more running-related transients during the trial. For each such GC recording, we calculated a tuning vector as the mean of the vectors pointing in the direction of the mouse's position at the time of each transient onset, inversely weighted by the mouse's occupancy of that position (Figures 2A, 2B, and S3). This vector's orientation and length defined the cell's tuning direction and tuning specificity, respectively. The mean spatial tuning specificity was significantly lower for abGCs than for mGCs (Figure 2C). We did not observe significant reward-related or velocity-related activity in our recordings (Figure S4).

To assess the statistical significance of the tuning specificity difference, for each GC we generated a null distribution by randomly shuffling calcium transient onset times and repeatedly recomputing the tuning specificity. This allowed us to calculate the p value as the fraction of this null distribution that exceeded the GC's tuning specificity. The p value distributions for both mGCs and abGCs differed significantly from chance levels, indicating that spatially tuned cells existed within both populations (Figure 2D). However, the p value distribution for mGC populations was lower than that for abGCs (Figure 2D), suggesting that as a population the mGCs demonstrate a higher degree of spatial tuning than abGCs. Across all significance thresholds, a higher fraction of mature neurons would be categorized as spatially tuned than of young neurons. These findings indicate that abGCs differ from mGCs not just in their level of activity but also in the spatial information carried by their activity.

To investigate whether the observed difference in spatial tuning was dependent on the value of our inclusion threshold, we compared the spatial tuning p values of mGCs and abGCs for different minimum numbers of running-related transients (Figure 2E). At all inclusion thresholds, mean p values were lower for mGCs than for abGCs. As expected for a population in which there was no relationship between spatial tuning and activity level, the p values for mGCs decreased monotonically with increasing inclusion threshold (statistical power increases, and hence p values decrease with greater numbers of transients). The lack

of a similar decrease in abGCs suggests a dependence of tuning on activity, whereby the most active abGCs tend to be least tuned (see Figure S3).

It is important to note that a lower tuning specificity could be consistent with an interpretation of multiple place fields, and a difference in this metric could either be attributable to inconsistent tuning or to tuning that is consistent but multipeaked or broader. Estimating the precise number of fields was not possible due to the sparsity of events observed. However, in order to account for the possibility of multipeaked tuning profiles, we also calculated the mutual information between the occupancy-normalized Ca^{2+} transient rate maps and the mouse's position. The traditional definition of spatial information (Skaggs et al., 1993), based on the method of sieves, is a highly biased estimator in the setting of sparse firing rates, as were observed in our data (Paninski, 2003), therefore it was not possible to quantify absolute spatial information rates in these cells. However, a p value analysis derived similarly to that of tuning specificity above is immune to this bias, since both the calculated and shuffled distributions are calculated in the same manner (see Experimental Procedures). This analysis, which is independent of the tuning specificity metric and does not inherently select for singly peaked tuning profiles, confirmed our primary results. Spatial information p values and tuning specificity p values were linearly related on a logarithmic scale, yielding largely overlapping populations of cells (Figures 4A and 4B). The spatial information p value distributions for both populations differed significantly from chance levels, but the mGC p value distribution was significantly lower than that of abGCs, again suggesting that as a population abGCs are relatively less spatially tuned (Figure 4C). We also observed a similar relationship between the minimum number of transients and the mean spatial information p value as was described in the tuning specificity analysis (Figure 4D). We saw no consistent evidence of multipeaked firing in the tuning profiles of recordings that satisfied the spatial information, but not the tuning specificity criterion. In summary, this spatial information-based analysis further supports our finding that as a population, abGCs are less sharply tuned than the mGC population.

Contextual Discrimination by abGCs and mGCs

We next assessed the context specificity of spatial representations within the population of spatially tuned mGCs and abGCs (Figure 3). We compared the similarity of GCs' spatial tuning between two sequential exposures to either similar ("A-B") or identical ("B-B") contexts. The similar contexts A and B shared the same treadmill belt but had different olfactory, auditory, visual, and tactile cues (Figure 3A). We focused our analysis on cells with significant and well-estimated spatial tuning (at least four running-related transients in both sessions and tuning specificity p value below 0.1 in at least one session; Figure 3B). Spatially tuned mGCs displayed a higher correlation of their tuning curves (Figures 3C, S5A, and S5B) and a smaller centroid shift (angle between tuning directions; Figures 3D, S5A, and S5B) in the B-B condition than in the A-B condition. The small number of spatially tuned abGCs satisfying the inclusion criteria displayed a significantly higher correlation of tuning curves in the B-B condition than in A-B, but this result did not hold for the centroid shift metric. When basing the inclusion criteria on the spatial information p value, rather than on the tuning specificity, we similarly observed that mGCs remapped to a greater degree in the A-B than the B-B conditions as assessed by both metrics (Figures 4E

and 4F). abGCs did not demonstrate a significant difference in remapping in the A-B versus B-B comparison, though it is important to note that this was difficult to assess given the low number of abGCs meeting the inclusion threshold. While the A-B-B paradigm allowed us to measure reorganization in response to the manipulation of a novel context, B-B-A and other related paradigms will allow for assessment of reorganization in a more familiar environment.

We next investigated whether DG GCs can discriminate between similar contexts solely on the basis of their activity level throughout the exposure to these contexts, which would be indicative of rate remapping (Figures 5, S5C, and S5D). To determine this, we computed population vectors (Figure 5A) whose components were the time-averaged calcium transient rate (Figure 5B) or the transient AUC rate (Figure 5C) for each cell during the trial. By measuring the angle between population vectors ($\Theta_{B\text{-}B}$, $\Theta_{A\text{-}B}$) we found that for both mGCs and abGCs the population vectors were as closely aligned between sequential exposures to the same (B-B) versus different (A-B) contexts. To control for the disparities in sample size between adult-born and mature populations, we studied the pseudopopulation vectors (Figure 5D) obtained by pooling GCs across all FOVs. The contextual specificity ($\Theta_{B\text{-}B} - \Theta_{A\text{-}B}$) for the abGC pseudopopulation fell well within the distribution obtained from random subsamplings of the mGC pseudopopulations for both the transient rate (Figure 5E) and transient AUC rate (Figure 5F) vectors. This indicates that in our experimental paradigm, both abGCs and mGCs discriminate between contexts at the level of their spatial tuning rather than through spatially independent changes in firing rate.

abGCs Actively Participate in the Encoding of Novel Information

Finally, we asked whether abGCs are required for encoding a novel environment. In order to address this question, we expressed *archaerhodopsin* (*Arch*) in abGCs by crossing the NestinCreER^{T2} mouse line with conditional Arch-eGFP mice (Madisen et al., 2012) (*Nestin*^{Arch}; Figure 6A). *Nestin*^{Arch} mice given TMX in adulthood expressed the transgene in ~80%–90% of abGCs in the DG (Figure S6). Targeted fiber optic implantation allowed local light delivery and thus control of 6-week-old and younger DG abGCs expressing Arch during behavior (Figure 6A). To examine effects on context encoding, mice received local illumination of the dorsal DG as they explored a conditioning context before receiving a single foot shock; they were then exposed to this same context 24 hr later in the absence of light. *Nestin*^{Arch} mice froze significantly less than control mice, indicating that activity in abGCs was required for effective contextual encoding (Figure 6B). Optical stimulation of abGCs impaired conditioning, presumably by disrupting the circuit (Figure S6). Optical modulation of abGCs did not impact shock reactivity, anxiety-related behavior, or general locomotor activity (Table S1).

We next tested whether transient inhibition of abGCs impacts behavioral pattern separation, the ability to discriminate between similar contexts, which has been proposed to require abGCs (Clelland et al., 2009; Kheirbek et al., 2012a; Nakashiba et al., 2012; Sahay et al., 2011a). We suppressed abGC activity either during exposure to the conditioning context A or to the similar, nonconditioned context B (Figures 6C and 6D). While silencing abGCs during exposure to the conditioning context did not impair the development of a

discriminatory response (Figure 6C), silencing these cells during exposure to the similar context resulted in impaired discrimination (Figure 6D), indicating that activity of the abGCs is required for behavioral pattern separation specifically during exposure to the ambiguous context. *Nestin*^{Arch} mice could discriminate between very distinct contexts and between similar contexts when silencing was performed after the mice had already learned to discriminate (Figure S6). Together, these data extend our understanding of the role played by abGCs during pattern separation on a behavioral level.

DISCUSSION

The results presented herein expand our understanding of the contribution of abGCs to the function of the DG. We found that activity was sparse in both the mGC and abGC populations, consistent with in vivo extracellular electrophysiological studies and intracellular recordings (Alme et al., 2010; Leutgeb et al., 2007; Pernía-Andrade and Jonas, 2014; Schmidt-Hieber et al., 2014). By monitoring for the first time in vivo the activity of this population of cells while mice explored multisensory contexts, we reveal that GCs 6 weeks and younger fire at a higher rate in vivo than the mature population, complementing recent findings showing that young GCs are more excitable in in vitro preparations (Marín-Burgin et al., 2012). In the absence of combined electrophysiological recordings, we cannot eliminate the possibility that transient differences in Ca^{2+} buffering might affect our activity estimates (Brandt et al., 2003), though we detected no consistent differences in the amplitude or duration of detected somatic Ca^{2+} transients (see also Marín-Burgin et al., 2012) at the FOV or individual mouse level.

We further found that abGCs were less spatially tuned than mGCs. The lower tuning specificity we observed could either be attributable to less stable spatial firing patterns or to the presence of stable but multipeaked tuning profiles, as might be expected from recent electrophysiological recordings describing broader, multipeaked tuning profiles at the hilar-GCL border, where most abGCs reside (Alme et al., 2010; Neunuebel and Knierim, 2012). In addition to a lower tuning specificity, however, we found that abGCs fire with relatively less spatial information. Although our behavioral paradigm did not allow for the systematic study of time coding (Kraus et al., 2013; MacDonald et al., 2011) in the GC population, we did not find that GC activity was related to other dimensions of the task, such as reward or velocity (Kropff et al., 2015).

Our results also suggested the existence of a relationship between activity and tuning in abGCs, in which the highly active abGCs are less spatially tuned. These results may be related to the maturational heterogeneity of the labeled cells and are consistent with a model in which young abGCs are initially more active and less spatially tuned but within 6 weeks become more similar to the less active and more spatially tuned mature cells. It is important to note that the *Nestin*^{tdTomato} labeling system does not provide an exact birthdate of the recorded neurons but rather results in the cumulative labeling of abGCs 6 weeks and younger. Consequently, we are unable to unequivocally distinguish abGCs between 0 and 6 weeks in our recordings. The recorded abGCs exhibited strong state-dependent modulation (Figure S2C), presumably driven by their glutamatergic innervation and local integration into the DG circuit. As both of these developmental events have been demonstrated to occur

after approximately 3 weeks of development (Espósito et al., 2005; Ge et al., 2006, 2007; Toni et al., 2007), this suggests that our functional characterization was based predominantly on cells in the 3–6 week age range. Future studies incorporating the imaging techniques described here with retroviral approaches for labeling age-matched cohorts of abGCs will allow for a more detailed determination of the developmental timeline of abGC properties in vivo. Such future studies will allow us to track (in the 3–6 week range) the transition from an immature to a mature functional phenotype.

Our in vivo imaging data suggest that the small population of spatially tuned abGCs differentiated novel contexts on the basis of their spatial tuning to a similar and possibly weaker degree than mGCs, depending on the metric and inclusion criteria applied. This, combined with the fact that we observed so few well-tuned abGCs in spite of our large number of recordings, suggests that the unique role of abGCs in contextual discrimination behaviors may not be attributable to the spatial distribution of their firing or the remapping of their fields. The broader tuning profile of abGCs (compared to mGCs) is consistent with computational models of GC dynamics and might support the encoding of novel features in the environment (Aimone et al., 2011; Temprana et al., 2015). This would also be consistent with our finding that silencing these neurons during exposure to the novel context (but not the familiar one) prevents contextual discrimination learning. Alternatively, the abGC population may modulate local excitatory/inhibitory tone in the DG and CA3 (Gu et al., 2012; Restivo et al., 2015; Toni et al., 2008) and could consequently shape spatial and contextual representations. There is indeed evidence from ablation studies that abGCs may modulate the activity of mGCs, possibly via their influence on the DG microcircuit (Burghardt et al., 2012; Drew et al., 2015; Ikrar et al., 2013; Lacefield et al., 2012; Park et al., 2015). Future studies should test this hypothesis directly by using the methods described here to assess changes in mGC spatial and contextual representations following inhibition of abGCs.

In addition, we find that transient inhibition of abGCs impairs behavior, specifically contextual encoding and discrimination, consistent with a proposed role in behavioral pattern separation (Clelland et al., 2009; Kheirbek et al., 2012a, 2012b; Nakashiba et al., 2012; Sahay et al., 2011a). These studies complement recent optogenetic studies describing a role for DG GCs in memory processes (Denny et al., 2014; Gu et al., 2012; Kheirbek et al., 2013). Furthermore, we demonstrate that in a pattern separation task, activity of the abGCs is required during exposure to the novel ambiguous context, but not during exposure to the conditioning context. This is likely due to a deficit in contextual encoding, due to an inability in $Nestin^{Arch}$ mice to encode context B as the safe context. This is in agreement with our results in one-trial contextual fear conditioning, where silencing abGCs during the first exposure to context A impaired the ability to encode this context. In the pattern separation experiment, when abGC silencing takes place in context A, freezing keeps increasing because learning is reinforced each day by a foot shock. In contrast, when silencing takes place in context B, freezing decreases in both contexts. This suggests that in these conditions, mice were confused when exposed to both contexts A and B and could no longer encode them as safe or fearful nor discriminate between them.

It is important to note that in this study, the behavior measured during optical inhibition of abGCs in contextual fear discrimination tasks differed from that in the head-fixed preparation during imaging. It was not possible for us to perform our behavioral and imaging experiments in identical conditions, as animals are known to freeze in response to an unconditioned stimulus in our head-fixed paradigm, and thus we cannot measure spatial tuning and remapping in a fear-conditioned animal. Future experiments combining freely moving in vivo imaging designs (Ziv et al., 2013) with behavioral pattern separation tasks will allow for analysis of changes in abGC response profiles to novel or conditioned contexts.

Our experimental preparation required a partial lesion of ipsilateral area CA1 in order to obtain high-resolution optical access to the DG. While DG-mediated behavior was normal in the experimental animals (Figures S1D and S1E), we cannot rule out the possibility that chronic circuit reorganization or the implementation of an alternate circuit strategy might occur in this preparation. Although the implant did not impact overall levels of neurogenesis, or the morphological features of recorded abGCs, we cannot exclude the possibility that the properties of abGCs and mGCs may be differentially affected by the surgical preparation, due, for example, to the potential disruption of grid cell activity in the medial entorhinal cortex (Bonnevie et al., 2013). In the future, less-invasive techniques should complement the results of this study.

Our data not only demonstrate the importance of abGCs for encoding and disambiguating contextual information but also provide insights into the circuit dynamics underlying these processes. Impairments in pattern separation have been proposed to contribute to the excessive generalization of memory often seen in anxiety and depression as well as in age-related disorders such as mild cognitive impairment (Kheirbek et al., 2012a; Leal et al., 2014; Yassa et al., 2011). A mechanistic understanding of how abGCs contribute to hippocampus-dependent memory processing will provide insights not only into the normal function of adult hippocampal neurogenesis but also into the therapeutic potential of this unique form of plasticity.

EXPERIMENTAL PROCEDURES

Full details of the experimental procedures are provided in the Supplemental Information.

Mice, Viruses, and Stereotactic Surgery

All experiments were conducted in accordance with the U.S. NIH guidelines and with the approval of the Columbia University and New York State Psychiatric Institute Institutional Animal Care and Use Committees. Male *Ai9*, *Ai35*, Nestin-CreER^{T2}, and controls were generated as previously described (Dranovsky et al., 2011; Madisen et al., 2010, 2012). For imaging experiments, recombinant adeno-associated viruses carrying the GCaMP6f gene were obtained from the Penn Vector Core (AAV1.Syn.GCaMP6f.WPRE.SV40) with titer of 2–4 × 10^{13}. The dorsal DG of male mice (8 weeks of age) was stereotactically injected at −1.5 mm AP; −2.3 mm ML; and −1.8, −1.65, −1.5 mm DV relative to the cortical surface. Mice were then surgically implanted with an imaging window over the left dorsal DG and implanted with a stainless-steel headpost for head fixation during imaging experiments (see

Supplemental Information). For optogenetic experiments, male mice (8 weeks of age) were surgically implanted with fiber optics targeted to the dorsal DG (±1 mm ML, −1.5 mm AP, −1.7 mm DV) using published protocols (Kheirbek et al., 2013).

In Vivo Two-Photon Imaging

We used the same imaging system as described previously (Kaifosh et al., 2013; Lovett-Barron et al., 2014), with the addition of an 8 kHz resonant galvanometer (Bruker). All images were acquired with a Nikon 40× NIR water-immersion objective (0.8 NA, 3.5 mm WD) in distilled water. We continuously acquired red (tdTomato) and green (GCaMP6f) channels separated by an emission cube set (green, HQ525/70 m-2p; red, HQ607/45 m-2p; 575dcxr, Chroma Technology) at 1024 × 1024 pixels covering 300 μm × 300 μm at 15 Hz with photomultiplier tubes (green GCaMP fluorescence, GaAsP PMT, Hamamatsu Model 7422P-40; red tdTomato fluorescence, multialkali PMT, Hamamatsu R3896). A custom dual stage preamp (1.4×10^5 dB, Bruker) was used to amplify signals prior to digitization.

For training, mice were water restricted (>90% predeprivation weight) and trained to run on a cue-deplete burlap treadmill belt for water reward over the course of 1–2 weeks. We applied a progressively restrictive water reward schedule, with mice initially receiving 40 randomly placed rewards per lap and ultimately receiving 3 randomly placed rewards per lap. Mice were habituated to the optical instrumentation, then trained for 20 min daily until they regularly ran at least one lap per minute. For contexts, similar to our previous work, each context (1 and 2) consisted of the same treadmill belt (the same sequence of three joined fabric ribbons) but was distinct in its visual, auditory, tactile, and olfactory stimuli (Figure 4A) (Lovett-Barron et al., 2014). During imaging sessions, mice received three randomly placed water rewards per lap, with reward positions changing randomly each lap. To allow for comparison of GC activity between similar contexts, the same three fabrics were used in the same order, but the locations of all of the tactile cues were shuffled between the two belts.

Imaging Analysis

Processing of Ca^{2+} Fluorescence Data—All imaging data were analyzed using the SIMA software package (Kaifosh et al., 2014). Motion correction was performed using a 2D Hidden Markov Model (Dombeck et al., 2007; Kaifosh et al., 2013), with modifications to accommodate the specific features of data acquired with resonant galvanometers. Only the green GCaMP channel was used for estimating motion artifacts. In cases where motion artifacts were not adequately corrected, the affected data were discarded from further analysis. The especially sparse activity of dentate GCs prevented the successful application of activity-based segmentation methods. Therefore, we used the SIMA project's ROI Buddy graphical user interface (Kaifosh et al., 2014) to draw regions of interest (ROIs) over GC somata visible in the time-averaged image of the motion-corrected green/GCaMP6f channel. We also used this software to determine the correspondence of ROIs across datasets from different trials in which the same FOV was imaged. To prevent the introduction of any bias, the red tdTomato channel was not viewed when drawing ROIs but only referenced after all ROIs had been drawn in order to tag ROIs over tdTomato-expressing cells as newborn GCs.

Dynamic GCaMP6f fluorescence signals were extracted from ROIs using SIMA according to the previously described formulation (Kaifosh et al., 2014). We then computed the relative fluorescence changes (ΔF/F) (as described in Jia et al., 2011), with uniform smoothing window t_1 = 3 s and baseline size t_2 = 60 s. We detected statistically significant calcium transients as described previously (Dombeck et al., 2007; Lovett-Barron et al., 2014). In order to improve our sensitivity, we then recalculated the baseline of the raw signal after masking frames identified previously as occurring during a significant transient. ΔF/F was then recalculated and transients re-estimated. Transients less than 1 s were removed to reduce false positives. This iterative procedure was repeated three times and effectively removed the transient contamination from the calculated baseline.

Spatial Tuning Vector and Tuning Specificity p Value Analysis—When evaluating the spatial tuning of GCs, we restricted our analysis to running-related epochs, defined as consecutive frames of forward locomotion (defined as an imaging frame in which at least one forward pair of beam breaks occurred) at least 1 s in duration and with a minimum peak speed of 5 cm/sec. Consecutive epochs separated by <0.5 s were merged. Running-related transients were defined as those that were initiated during a running-related epoch. Transient start was defined as the first imaging frame with mean fluorescence ≥2 σ, with σ equal to the SD of the baseline frames. Offset was defined as the first frame with mean fluorescence ≤0.5 σ (Dombeck et al., 2007). The spatial tuning vector was calculated as $\sum_{\mathrm{j}} \frac{e^{i\theta_j}}{o\,(\theta_j)}$, where θ_j is the position of the mouse at the onset time of the j[th] running-related transient, and o_j is the fraction of running frames acquired at position θ_j. Only the animal's position at the time of transient onset was used for constructing the tuning vector and rate maps (see Remapping Analysis section below), as the calcium decay kinetics are intrinsic to the GCaMP6f indicator and are not sensitive to the animal's running speed (a similar onset-based approach was implemented previously by Ziv et al., 2013). In order to assess the significance of the spatial selectivity, for each cell we generated a null tuning distribution by shuffling the transient onset times (restricted to running frames) and repeatedly recomputing the tuning specificity. This process was repeated 100,000 times, and the p value was defined as the fraction of this distribution that exceeded the GC's tuning specificity.

Spatial Information p Value Analysis—For each cell we first computed the spatial information content (Skaggs et al., 1993) as $I_N = \sum_{i=1}^{N} \lambda_i \, ln \frac{\lambda_i}{\lambda} p_i$, where λ_i and p_i are the transient rate and fraction of time spent in the i th bin, λ is the overall firing rate, and N is the number of bins. We computed I_N for multiple values of N = 2, 4, 5, 8, 10, 20, 25, and 100. We then created 100,000 random reassignments of the transient onset times within the running-related epochs and recomputed the values of I_N^s, where s is the index of the shuffle. To roughly correct for biases in the calculation of mutual information, we then subtracted the mean of this null distribution from all estimates to obtain values $\hat{I}_N = I_N - \frac{1}{100,000} \sum_{s=1}^{100,000} I_N^s$. Finally, we computed a single estimate of the information content for the true transient onset times, $\hat{I} = max_N \hat{I}_N$, and for the shuffles, $\hat{I}_s = max_N \hat{I}_N^s$. The spatial tuning p value was taken as the fraction of values of s for which $\hat{I}$ exceeded $\hat{I}_s$.

Remapping Analysis—Rate maps were formed by dividing the number of transients starting in each bin by the occupancy of that bin. We calculated rate maps with 100 position bins and smoothed with a Gaussian kernel ($\sigma = 3$ bins). The tuning curve correlation for each cell was defined as the Pearson correlation coefficient between tuning curves for a cell in the two sequential context exposures. The centroid shift for each cell was defined as the angle (in radians) between the tuning directions calculated for the two context exposures. For both metrics, the shuffle distributions were calculated by estimating the tuning curve correlations or tuning shifts when cells were paired by a subsampled Cartesian product of cell identities (1,000 pairs per shuffle).

Behavioral Testing

In Arch experiments, the patch cables were interfaced to an FC/PC rotary joint (Doric lenses), which was attached on the other end to a 593.5 nm laser diode that was controlled by a Master-8 stimulator (AMPI). Fear conditioning took place in Coulbourn Instruments fear conditioning boxes. See Supplemental Information for full details of behavioral procedures.

Statistics

For all optogenetic behavioral data, data were analyzed using ANOVA with repeated measurements where appropriate. All tests are described in the appropriate figure legends. Group numbers were based on previous optogenetic and two-photon imaging experiments (Kheirbek et al., 2013; Lovett-Barron et al., 2014). For imaging data, for all normally distributed data, a Welch's two-sample t test was used for comparison of means with n – 1 degrees of freedom. The Mann-Whitney U test was used for comparison of means in non-normally distributed data with n – 1 degrees of freedom. A paired student's t test was used for comparison of means in paired data with n – 1 degrees of freedom. The one-sided Kolmogorov-Smirnov (KS) test was used for testing the hypothesis that a distribution was drawn from an underlying theoretical distribution with n – 1 degrees of freedom (uniformity in the case of Figure 2E). The two-sided two-sample KS test with n – 1 degrees of freedom was used for testing the null hypothesis that two empirical distributions were drawn from the same continuous underlying distribution.

Supplementary Material

Refer to Web version on PubMed Central for supplementary material.

ACKNOWLEDGMENTS

We thank L. Looger, S. Fusi, and A. Fenton for discussion and comments; H. Zeng for Ai32 and Ai35 mice; and the GENIE Program at the Janelia Farm Research Campus for GCaMP6f. N.B.D is supported by NINDS F30NS090819. P.K. is a Howard Hughes Medical Institute International Pre-doctoral Fellow. M.L.-B. was supported by a Canadian Natural Sciences and Engineering Research Council postgraduate scholarship. A.L. is supported by NIMH 1R01MH100631, 1U01NS090583, 1R01NS094668, the Searle Scholars Program, the Human Frontier Science Program, and the McKnight Memory and Cognitive Disorders Award. R.H. is supported by NIH R37 MH068542, NIA R01 AG043688, New York State Stem Cell Science (NYSTEM), and the Hope for Depression Research Foundation. M.A.K. was supported by NIMH K01MH099371, NARSAD, and NYSTEM.

REFERENCES

Aimone JB, Deng W, Gage FH. Resolving new memories: a critical look at the dentate gyrus, adult neurogenesis, and pattern separation. Neuron. 2011; 70:589–596. [PubMed: 21609818]

Alme CB, Buzzetti RA, Marrone DF, Leutgeb JK, Chawla MK, Schaner MJ, Bohanick JD, Khoboko T, Leutgeb S, Moser EI, et al. Hippocampal granule cells opt for early retirement. Hippocampus. 2010; 20:1109–1123. [PubMed: 20872737]

Bonnevie T, Dunn B, Fyhn M, Hafting T, Derdikman D, Kubie JL, Roudi Y, Moser EI, Moser MB. Grid cells require excitatory drive from the hippocampus. Nat. Neurosci. 2013; 16:309–317. [PubMed: 23334581]

Brandt MD, Jessberger S, Steiner B, Kronenberg G, Reuter K, Bick-Sander A, von der Behrens W, Kempermann G. Transient calretinin expression defines early postmitotic step of neuronal differentiation in adult hippocampal neurogenesis of mice. Mol. Cell. Neurosci. 2003; 24:603–613. [PubMed: 14664811]

Burghardt NS, Park EH, Hen R, Fenton AA. Adult-born hippocampal neurons promote cognitive flexibility in mice. Hippocampus. 2012; 22:1795–1808. [PubMed: 22431384]

Clelland CD, Choi M, Romberg C, Clemenson GD Jr. Fragniere A, Tyers P, Jessberger S, Saksida LM, Barker RA, Gage FH, Bussey TJ. A functional role for adult hippocampal neurogenesis in spatial pattern separation. Science. 2009; 325:210–213. [PubMed: 19590004]

David DJ, Samuels BA, Rainer Q, Wang JW, Marsteller D, Mendez I, Drew M, Craig DA, Guiard BP, Guilloux JP, et al. Neurogenesis-dependent and -independent effects of fluoxetine in an animal model of anxiety/depression. Neuron. 2009; 62:479–493. [PubMed: 19477151]

Denny CA, Burghardt NS, Schachter DM, Hen R, Drew MR. 4- to 6-week-old adult-born hippocampal neurons influence novelty-evoked exploration and contextual fear conditioning. Hippocampus. 2012; 22:1188–1201. [PubMed: 21739523]

Denny CA, Kheirbek MA, Alba EL, Tanaka KF, Brachman RA, Laughman KB, Tomm NK, Turi GF, Losonczy A, Hen R. Hippocampal memory traces are differentially modulated by experience, time, and adult neurogenesis. Neuron. 2014; 83:189–201. [PubMed: 24991962]

Dieni CV, Nietz AK, Panichi R, Wadiche JI, Overstreet-Wadiche L. Distinct determinants of sparse activation during granule cell maturation. J. Neurosci. 2013; 33:19131–19142. [PubMed: 24305810]

Dombeck DA, Khabbaz AN, Collman F, Adelman TL, Tank DW. Imaging large-scale neural activity with cellular resolution in awake, mobile mice. Neuron. 2007; 56:43–57. [PubMed: 17920014]

Dranovsky A, Picchini AM, Moadel T, Sisti AC, Yamada A, Kimura S, Leonardo ED, Hen R. Experience dictates stem cell fate in the adult hippocampus. Neuron. 2011; 70:908–923. [PubMed: 21658584]

Drew LJ, Fusi S, Hen R. Adult neurogenesis in the mammalian hippocampus: why the dentate gyrus? Learn. Mem. 2013; 20:710–729. [PubMed: 24255101]

Drew LJ, Kheirbek MA, Luna VM, Denny CA, Cloidt MA, Wu MV, Jain S, Scharfman HE, Hen R. Activation of local inhibitory circuits in the dentate gyrus by adult-born neurons. Hippocampus. 2015 Published online December 14, 2015. http://dx.doi.org/10.1002/hipo.22557.

Espósito MS, Piatti VC, Laplagne DA, Morgenstern NA, Ferrari CC, Pitossi FJ, Schinder AF. Neuronal differentiation in the adult hippocampus recapitulates embryonic development. J. Neurosci. 2005; 25:10074–10086. [PubMed: 16267214]

Ge S, Goh EL, Sailor KA, Kitabatake Y, Ming GL, Song H. GABA regulates synaptic integration of newly generated neurons in the adult brain. Nature. 2006; 439:589–593. [PubMed: 16341203]

Ge S, Yang CH, Hsu KS, Ming GL, Song H. A critical period for enhanced synaptic plasticity in newly generated neurons of the adult brain. Neuron. 2007; 54:559–566. [PubMed: 17521569]

Gu Y, Arruda-Carvalho M, Wang J, Janoschka SR, Josselyn SA, Frankland PW, Ge S. Optical controlling reveals time-dependent roles for adult-born dentate granule cells. Nat. Neurosci. 2012; 15:1700–1706. [PubMed: 23143513]

Ikrar T, Guo N, He K, Besnard A, Levinson S, Hill A, Lee HK, Hen R, Xu X, Sahay A. Adult neurogenesis modifies excitability of the dentate gyrus. Front. Neural Circuits. 2013; 7:204. [PubMed: 24421758]

Imayoshi I, Sakamoto M, Ohtsuka T, Takao K, Miyakawa T, Yamaguchi M, Mori K, Ikeda T, Itohara S, Kageyama R. Roles of continuous neurogenesis in the structural and functional integrity of the adult forebrain. Nat. Neurosci. 2008; 11:1153–1161. [PubMed: 18758458]

Jia H, Rochefort NL, Chen X, Konnerth A. In vivo two-photon imaging of sensory-evoked dendritic calcium signals in cortical neurons. Nat. Protoc. 2011; 6:28–35. [PubMed: 21212780]

Jung MW, McNaughton BL. Spatial selectivity of unit activity in the hippocampal granular layer. Hippocampus. 1993; 3:165–182. [PubMed: 8353604]

Kaifosh P, Lovett-Barron M, Turi GF, Reardon TR, Losonczy A. Septo-hippocampal GABAergic signaling across multiple modalities in awake mice. Nat. Neurosci. 2013; 16:1182–1184. [PubMed: 23912949]

Kaifosh P, Zaremba JD, Danielson NB, Losonczy A. SIMA: Python software for analysis of dynamic fluorescence imaging data. Front. Neuroinform. 2014; 8:80. [PubMed: 25295002]

Kheirbek MA, Klemenhagen KC, Sahay A, Hen R. Neurogenesis and generalization: a new approach to stratify and treat anxiety disorders. Nat. Neurosci. 2012a; 15:1613–1620. [PubMed: 23187693]

Kheirbek MA, Tannenholz L, Hen R. NR2B-dependent plasticity of adult-born granule cells is necessary for context discrimination. J. Neurosci. 2012b; 32:8696–8702. [PubMed: 22723709]

Kheirbek MA, Drew LJ, Burghardt NS, Costantini DO, Tannenholz L, Ahmari SE, Zeng H, Fenton AA, Hen R. Differential control of learning and anxiety along the dorsoventral axis of the dentate gyrus. Neuron. 2013; 77:955–968. [PubMed: 23473324]

Kraus BJ, Robinson RJ 2nd, White JA, Eichenbaum H, Hasselmo ME. Hippocampal “time cells”: time versus path integration. Neuron. 2013; 78:1090–1101. [PubMed: 23707613]

Kropff E, Carmichael JE, Moser MB, Moser EI. Speed cells in the medial entorhinal cortex. Nature. 2015; 523:419–424. [PubMed: 26176924]

Lacefield CO, Itskov V, Reardon T, Hen R, Gordon JA. Effects of adult-generated granule cells on coordinated network activity in the dentate gyrus. Hippocampus. 2012; 22:106–116. [PubMed: 20882540]

Leal SL, Tighe SK, Jones CK, Yassa MA. Pattern separation of emotional information in hippocampal dentate and CA3. Hippocampus. 2014; 24:1146–1155. [PubMed: 24796287]

Leutgeb JK, Leutgeb S, Moser MB, Moser EI. Pattern separation in the dentate gyrus and CA3 of the hippocampus. Science. 2007; 315:961–966. [PubMed: 17303747]

Lovett-Barron M, Kaifosh P, Kheirbek MA, Danielson N, Zaremba JD, Reardon TR, Turi GF, Hen R, Zemelman BV, Losonczy A. Dendritic inhibition in the hippocampus supports fear learning. Science. 2014; 343:857–863. [PubMed: 24558155]

MacDonald CJ, Lepage KQ, Eden UT, Eichenbaum H. Hippocampal “time cells” bridge the gap in memory for discontiguous events. Neuron. 2011; 71:737–749. [PubMed: 21867888]

Madisen L, Zwingman TA, Sunkin SM, Oh SW, Zariwala HA, Gu H, Ng LL, Palmiter RD, Hawrylycz MJ, Jones AR, et al. A robust and high-throughput Cre reporting and characterization system for the whole mouse brain. Nat. Neurosci. 2010; 13:133–140. [PubMed: 20023653]

Madisen L, Mao T, Koch H, Zhuo JM, Berenyi A, Fujisawa S, Hsu YW, Garcia AJ 3rd, Gu X, Zanella S, et al. A toolbox of Cre-dependent optogenetic transgenic mice for light-induced activation and silencing. Nat. Neurosci. 2012; 15:793–802. [PubMed: 22446880]

Marín-Burgin A, Mongiat LA, Pardi MB, Schinder AF. Unique processing during a period of high excitation/inhibition balance in adult-born neurons. Science. 2012; 335:1238–1242. [PubMed: 22282476]

Nakashiba T, Cushman JD, Pelkey KA, Renaudineau S, Buhl DL, McHugh TJ, Rodriguez Barrera V, Chittajallu R, Iwamoto KS, McBain CJ, et al. Young dentate granule cells mediate pattern separation, whereas old granule cells facilitate pattern completion. Cell. 2012; 149:188–201. [PubMed: 22365813]

Neunuebel JP, Knierim JJ. Spatial firing correlates of physiologically distinct cell types of the rat dentate gyrus. J. Neurosci. 2012; 32:3848–3858. [PubMed: 22423105]

Paninski L. Estimation of entropy and mutual information. Neural Comput. 2003; 15:1191–1253.

Park EH, Burghardt NS, Dvorak D, Hen R, Fenton AA. Experience-dependent regulation of dentate gyrus excitability by adult-born granule cells. J. Neurosci. 2015; 35:11656–11666. [PubMed: 26290242]

Pernía-Andrade AJ, Jonas P. Theta-gamma-modulated synaptic currents in hippocampal granule cells in vivo define a mechanism for network oscillations. Neuron. 2014; 81:140–152. [PubMed: 24333053]

Piatti VC, Ewell LA, Leutgeb JK. Neurogenesis in the dentate gyrus: carrying the message or dictating the tone. Front. Neurosci. 2013; 7:50. [PubMed: 23576950]

Restivo L, Niibori Y, Mercaldo V, Josselyn SA, Frankland PW. Development of adult-generated cell connectivity with excitatory and inhibitory cell populations in the hippocampus. J. Neurosci. 2015; 35:10600–10612. [PubMed: 26203153]

Sahay A, Scobie KN, Hill AS, O'Carroll CM, Kheirbek MA, Burghardt NS, Fenton AA, Dranovsky A, Hen R. Increasing adult hippo-campal neurogenesis is sufficient to improve pattern separation. Nature. 2011a; 472:466–470. [PubMed: 21460835]

Sahay A, Wilson DA, Hen R. Pattern separation: a common function for new neurons in hippocampus and olfactory bulb. Neuron. 2011b; 70:582–588. [PubMed: 21609817]

Santarelli L, Saxe M, Gross C, Surget A, Battaglia F, Dulawa S, Weisstaub N, Lee J, Duman R, Arancio O, et al. Requirement of hippocampal neurogenesis for the behavioral effects of antidepressants. Science. 2003; 301:805–809. [PubMed: 12907793]

Schmidt-Hieber C, Jonas P, Bischofberger J. Enhanced synaptic plasticity in newly generated granule cells of the adult hippocampus. Nature. 2004; 429:184–187. [PubMed: 15107864]

Schmidt-Hieber, C.; Wei, H.; Hausser, M. Synaptic mechanisms of sparse activity in hippocampal granule cells during mouse navigation (Society for Neuroscience). 2014.

Singer BH, Gamelli AE, Fuller CL, Temme SJ, Parent JM, Murphy GG. Compensatory network changes in the dentate gyrus restore long-term potentiation following ablation of neurogenesis in young-adult mice. Proc. Natl. Acad. Sci. USA. 2011; 108:5437–5442. [PubMed: 21402918]

Skaggs, WE.; McNaughton, BL.; Gothard, KM.; Markus, EJ. An information-theoretic approach to deciphering the hippocampal code. In: Hanson, SJ.; Cowan, JD.; Giles, CL., editors. Advances in Neural Information Processing Systems (NIPS). Vol. 5. 1993. p. 1030-1037.

Snyder JS, Soumier A, Brewer M, Pickel J, Cameron HA. Adult hippocampal neurogenesis buffers stress responses and depressive behaviour. Nature. 2011; 476:458–461. [PubMed: 21814201]

Spalding KL, Bergmann O, Alkass K, Bernard S, Salehpour M, Huttner HB, Boström E, Westerlund I, Vial C, Buchholz BA, et al. Dynamics of hippocampal neurogenesis in adult humans. Cell. 2013; 153:1219–1227. [PubMed: 23746839]

Stone SS, Teixeira CM, Zaslavsky K, Wheeler AL, Martinez-Canabal A, Wang AH, Sakaguchi M, Lozano AM, Frankland PW. Functional convergence of developmentally and adult-generated granule cells in dentate gyrus circuits supporting hippocampus-dependent memory. Hippocampus. 2011; 21:1348–1362. [PubMed: 20824726]

Temprana SG, Mongiat LA, Yang SM, Trinchero MF, Alvarez DD, Kropff E, Giacomini D, Beltramone N, Lanuza GM, Schinder AF. Delayed coupling to feedback inhibition during a critical period for the integration of adult-born granule cells. Neuron. 2015; 85:116–130. [PubMed: 25533485]

Toni N, Teng EM, Bushong EA, Aimone JB, Zhao C, Consiglio A, van Praag H, Martone ME, Ellisman MH, Gage FH. Synapse formation on neurons born in the adult hippocampus. Nat. Neurosci. 2007; 10:727–734. [PubMed: 17486101]

Toni N, Laplagne DA, Zhao C, Lombardi G, Ribak CE, Gage FH, Schinder AF. Neurons born in the adult dentate gyrus form functional synapses with target cells. Nat. Neurosci. 2008; 11:901–907. [PubMed: 18622400]

van Praag H, Schinder AF, Christie BR, Toni N, Palmer TD, Gage FH. Functional neurogenesis in the adult hippocampus. Nature. 2002; 415:1030–1034. [PubMed: 11875571]

Yassa MA, Mattfeld AT, Stark SM, Stark CE. Age-related memory deficits linked to circuit-specific disruptions in the hippocampus. Proc. Natl. Acad. Sci. USA. 2011; 108:8873–8878. [PubMed: 21555581]

Zhao C, Deng W, Gage FH. Mechanisms and functional implications of adult neurogenesis. Cell. 2008; 132:645–660. [PubMed: 18295581]

Ziv Y, Burns LD, Cocker ED, Hamel EO, Ghosh KK, Kitch LJ, El Gamal A, Schnitzer MJ. Long-term dynamics of CA1 hippocampal place codes. Nat. Neurosci. 2013; 16:264–266. [PubMed: 23396101]

Highlights

- Ca^{2+} imaging of DG GCs in vivo indicates abGCs are more active than mGCs
- abGCs are less spatially tuned than mGCs
- Spatially tuned mGCs and abGCs remap spatial representations to a similar degree
- abGCs actively participate in the encoding of novel information

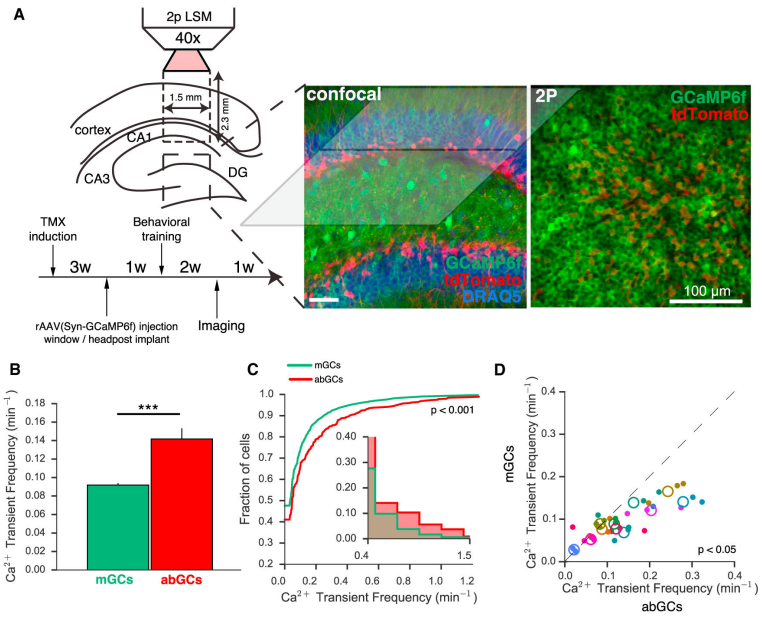

Figure 1. Functional Imaging of abGCs and mGCs

(A) Left: experimental schematic. Two-photon line-scanning microscopy allows for the recording of large populations of GCs in surgically exposed dorsal DG. Experimental timeline as indicated. Middle: confocal image of recovered tissue illustrating the geometry of the preparation. GCs (stained with DRAQ5) express GCaMP6f, with abGCs also expressing tdTomato. Right: time-averaged in vivo two-photon image of a representative FOV (300 × 300 µm), containing ~1,000 GCs.

(B) abGCs exhibit a higher rate of running-related calcium transients than mGCs ($p < 0.001$; n = 7,950 mGCs, 446 abGCs across 11 FOV in 6 mice; Welch's t test, $t_{(8,396)} = -4.14$; each measure is the average of 1–3 recordings for that cell).

(C) Distribution of firing rates across abGCs and mGCs demonstrates significantly different population-level activity ($p < 0.001$; Kolmogorov-Smirnov (KS) test, KS Stat = 0.10).

(D) Scatter of mean abGC and mGC running-related firing rates within each recording session (closed circles) and averaged across sessions for each FOV (open circles). Color reflects FOV as specified in Figure S6. Across imaging fields abGCs were significantly more active than mGCs ($p < 0.05$; n = 11 FOV; paired t test, $t_{(20)} = 2.88$). The same results were obtained when including all transients (data not shown).

Error bars are mean ± SEM.

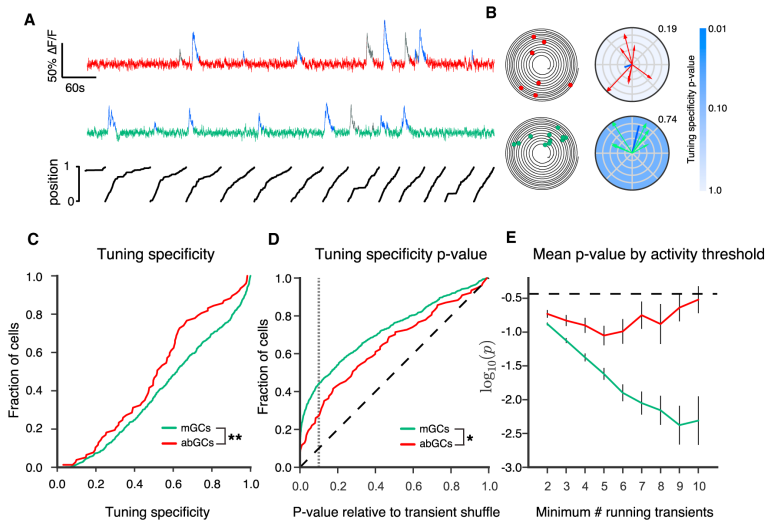

Figure 2. Spatial Tuning of abGCs and mGCs

(A) Time series of calcium signals from an example abGC (red) and mGC (green), with position of the mouse along the circular treadmill belt plotted below. Running-related calcium transients are indicated in blue (all others in gray).

(B) Left: trajectory plot of position (angular coordinate) and time (radial coordinate) with running-related calcium transients as dots along the trajectory. Right: spatial tuning plots for example mGC (green) and abGC (red). Vectors indicate the animal's position at the time of each running-related transient onset, with magnitude determined by the inverse of the fraction of time spent at that position. Blue lines indicate the calculated tuning vectors, whose orientation and magnitude correspond to the tuning direction and specificity, respectively. Tuning specificity is given next to each plot. Tuning specificity p value is indicated by blue shading.

(C) Cumulative distributions of tuning specificity values for active mGCs and abGCs (≥ four running-related transients). The abGC distribution was significantly left shifted as compared to the mGC distribution with few sharply tuned cells ($p < 0.01$; n = 639 mGCs, 77 abGCs from 11 FOVs in 6 mice; two-sample KS Test, KS Stat = 0.217, $p < 0.01$).

(D) Cumulative distributions of tuning specificity p values. The p value distributions for mGCs and abGCs differed significantly from each other ($p < 0.05$; KS test, KS Stat = 0.18) and from the uniform distribution (diagonal dashed line) expected in the case of a nonspatially tuned population ($p < 0.001$ for both mGCs and abGCs; KS test, abGCs, KS Stat = 0.25, mGCs KS Stat = 0.35). Gray dashed line indicates p = 0.1.

(E) Mean logarithm of the p value for mGCs and abGCs with differing inclusion thresholds for the number of running-related calcium transients. For mGCs, the p values monotonically decrease with increasing inclusion threshold, consistent with the increased statistical power provided by a greater numbers of transients. The lack of such a decrease in the adult-born population suggests that the more active abGCs tend to be less tuned or consist of a mixed population of tuned and untuned cells. The dashed black line shows the expected value for an untuned population.

Error bars are mean ± SEM.

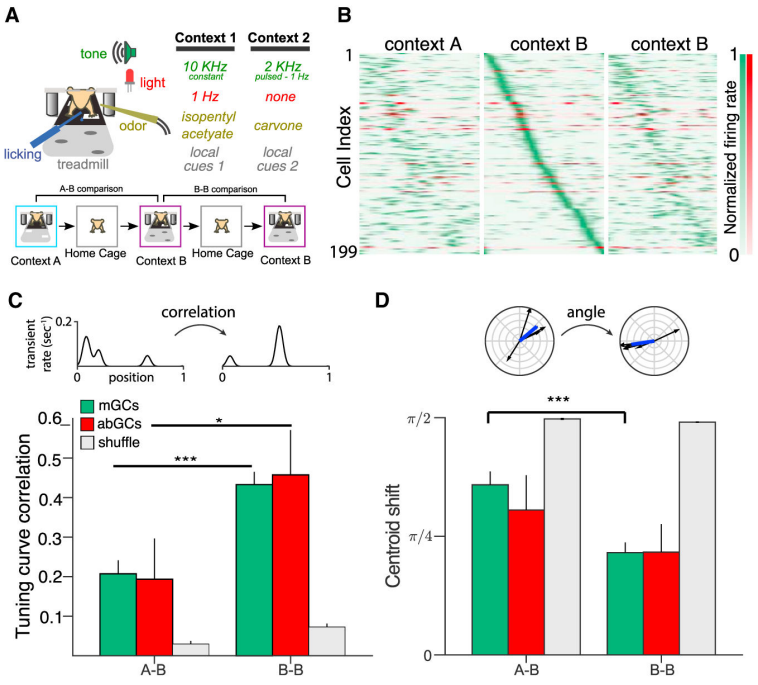

Figure 3. Contextual Coding by abGCs and mGCs

(A) Experimental schematic. Mice ran for three 12 min sessions in contexts A, B, and B (1 hr between runs). A and B refer to either context 1 or 2 (chosen randomly for each experiment).

(B) Remapping of spatial rate maps across sequential context exposures. Smoothed calcium transient rates, normalized to peak for each cell, are plotted as a function of position during three contextual exposures (A, B, B). Cells (mGCs, green; abGCs, red) are ordered according to the position of peak activity during the first exposure to context B. Data is shown for GCs with sufficient tuning specificity and activity ($p < 0.1$, at least four transients) in at least one experiment.

(C and D) Context specificity of spatial representations. Tuning curve correlations of 1D rate maps (C) and centroid shifts (angle between tuning directions) (D) between sequential exposures to different (A-B) or the same (B-B) contexts for all cells shown in (B) (A-B: n = 180 mGCs, 14 abGCs; B-B: n = 174 mGCs, 9 abGCs). The rate map correlations of both populations were more similar in the B-B condition than in A-B (Mann-Whitney U, mGCs: $U_{(150)} = 5{,}291$, $p < 0.001$; abGCs: $U_{(18)} = 23.0$, $p < 0.05$). In mGCs the tuning shift was larger in the A-B condition than in B-B, although this did not reach significance in abGCs (mGCs: $U_{(150)} = 5{,}714$, $p < 0.001$; abGCs: $U_{(18)} = 40.0$, $p = 0.34$). In both conditions, the similarity of spatial representations exceeded chance levels as estimated by shuffling cell identity (gray).

Error bars are mean ± SEM.

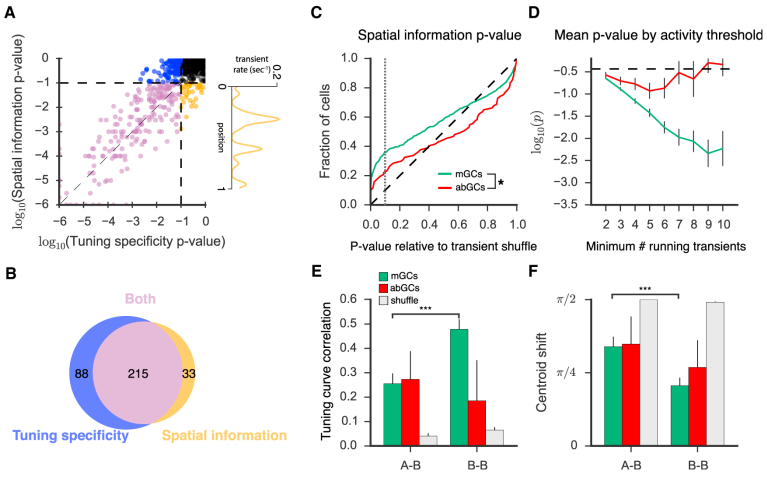

Figure 4. Spatial Information in abGCs

(A) For each cell firing at least four running-related transients, we calculated the spatial information p value and tuning specificity p value by shuffling the events in time and repeatedly recalculating either corresponding metric. Values are highly correlated on a log scale (r = 0.91, Pearson's R). Cells are colored according to whether they met the tuning specificity p value inclusion criterion only (blue), the spatial information p value criterion only (gold), both (purple), and neither (black). Right panel: the tuning profile of a cell meeting the spatial information, but not the tuning specificity, criteria is shown.

(B) Venn diagram demonstrates overlap in populations meeting the two inclusion criteria ($p < 0.10$).

(C) Cumulative distributions of spatial information p values. The p value distributions for mGCs and abGCs differed significantly from each other (KS test, KS Stat = 0.17, $p < 0.05$) and from the uniform distribution (diagonal dashed line) expected in the case of a nonspatially tuned population (KS test; mGCs: KS Stat = 0.26, $p < 0.001$; abGCs: KS Stat = 0.146, $p < 0.05$;). Gray dashed line indicates $p = 0.1$.

(D) Mean logarithm of the p value for mGCs and abGCs with differing inclusion thresholds for the number of running-related calcium transients. A similar relationship is seen as described in Figure 2E.

(E and F) Contextual discrimination analysis with inclusion criteria based on spatial information p value. For mGCs (A-B, n = 100; B-B, n = 106) the tuning curve correlation (E; Mann-Whitney U, $U_{(204)} = 3{,}597$, $p < 0.001$) and centroid shift (F; Mann-Whitney U, $U_{(204)} = 3{,}798$, $p < 0.001$) were both significantly more similar in the B-B condition than in A-B. This relationship was not observed (Mann-Whitney U; E; $U_{(14)} = 26.0$, $p = 0.45$; F; $U_{(14)} = 23.0$, $p = 0.32$) in the few abGCs (A-B, n = 11; B-B, n = 5) meeting the spatial information inclusion criterion.

Error bars are mean ± SEM.

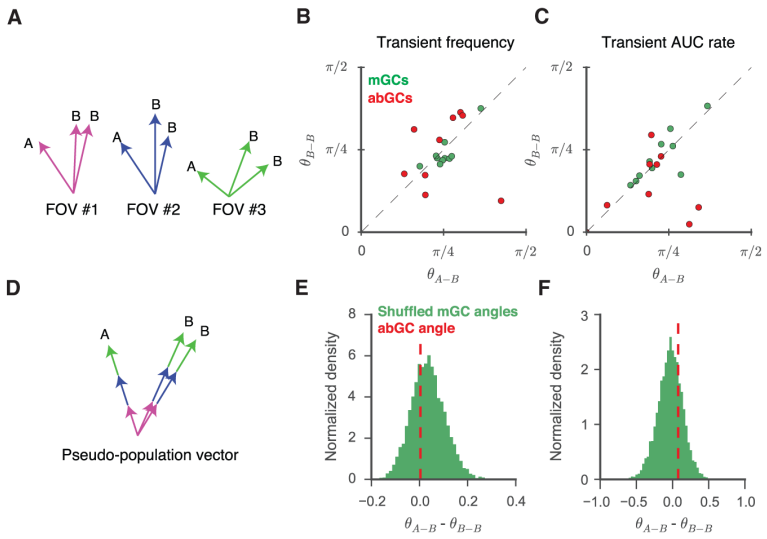

Figure 5. Mean Activity in GCs Does Not Code for Context

(A) Schematic of population vector analysis. Activity-based vectors were defined for each experiment, and angles were measured between sequential exposures to the same ($\theta_{B\text{-}B}$) or similar ($\theta_{A\text{-}B}$) contexts.

(B and C) Scatter of population vector angles across the two conditions in which vector components are defined as transient frequency (B) or rate of transient AUC (area under the curve of significant Ca^{2+} transients divided by the total time) (C). Each point corresponds to mature (green) or newborn (red) cells from one FOV. For neither abGC (B; paired t test, $T_{(16)} = 0.04$, $p = 0.97$; C; $T_{(16)} = 1.25$, $p = 0.25$) nor mGC (B; $T_{(18)} = 1.53$, $p = 0.16$; C; $T_{(18)} = 0.32$, $p = 0.76$) populations were the vectors more similar for sequential exposures to the same context than for sequential exposures to different contexts.

(D) For each contextual exposure, we calculated a single pseudopopulation vector by concatenating the newborn population vectors from all FOVs. Schematic is drawn to illustrate the case of activity-based discrimination.

(E and F) Lack of evidence for activity-based discrimination ($\theta_{A\text{-}B} - \theta_{B\text{-}B}$) for either transient frequency (E) and transient AUC rate (F). The dotted red line indicates the difference in the angles between the abGC pseudopopulation vectors. The difference was consistent with the distribution (green histogram) of such differences attained by repeatedly randomly downsampling similarly constructed pseudopopulations of mature cells (E, percentile = 34; F, percentile = 73; see Experimental Procedures).

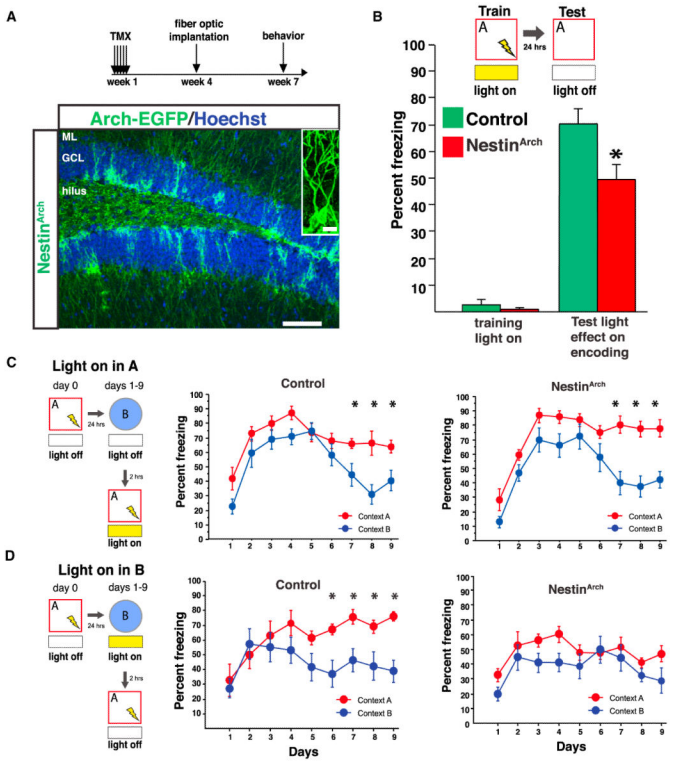

Figure 6. abGCs Participate in Memory Encoding and Discrimination

(A) Experimental design. Right: expression of Arch in abGCs (Scale bar, 100 μm; inset, 10 μm).

(B) Yellow-light inhibition of dorsal abGCs during training impaired encoding of contextual fear (n = 8 control, 9 Nestin^{Arch}; group effect $F_{(1,15)} = 6.3$, $p = 0.02$; groupXtraining interaction $F_{(1,15)} = 5.4$, $p = 0.03$; on test day $t_{15} = -2.5$, $p = 0.02$).

(C and D) Acute inhibition of abGCs impairs behavioral pattern separation. (C) Mice discriminated when abGCs were inhibited in the conditioning context (n = 7 control, 8 Nestin^{Arch}; groupXdayXcontext interaction $F_{(8,208)} = 0.581$, $p = 0.79$. Control: context effect $F_{(1,12)} = 7.243$, $p = 0.02$; dayXcontext interaction $F_{(8,96)} = 2.094$, $p = 0.0436$. Nestin^{Arch}: context effect $F_{(1,14)} = 10.631$, $p = 0.006$; dayXcontext effect $F_{(8,112)} = 3.706$, $p = 0.007$.).

(D) Mice did not discriminate when abGCs were inhibited in the unconditioned context (n = 8 control, 7 Nestin^{Arch}; groupXdayXcontext interaction $F_{(8,208)} = 1.9$, $p = 0.04$. Control: context effect $F_{(1,13)} = 4.8$, $p = 0.04$; dayXcontext interaction $F_{(8,104)} = 3.1$, $p = 0.004$. Nestin^{Arch}: context effect $F_{(1,12)} = 4.1$, $p = 0.06$; dayXcontext effect $F_{(8,96)} = 0.6$, $p = 0.74$). Error bars are mean ± SEM.